Steel and Composite Structures, *Vol. 35, No. 1* (*2020*) *77-92*
DOI: https://doi.org/10.12989/scs.2020.35.1.077

Geometrically nonlinear dynamic analysis of FG graphene platelets-reinforced nanocomposite cylinder: MLPG method based on a modified nonlinear micromechanical model

Mohammad Hossein Ghadiri Rad*[1], Farzad Shahabian[2a] and Seyed Mahmoud Hosseini[3b]

[1]*Civil Engineering Department, Quchan University of Technology, Quchan, Iran*
[2]*Civil Engineering Department, Faculty of Engineering, Ferdowsi University of Mashhad, Mashhad, Iran*
[3]*Industrial Engineering Department, Faculty of Engineering, Ferdowsi University of Mashhad, Mashhad, Iran*

(*Received September 24, 2019, Revised December 30, 2019, Accepted January 10, 2020*)

Abstract. The present paper outlined a procedure for geometrically nonlinear dynamic analysis of functionally graded graphene platelets-reinforced (GPLR-FG) nanocomposite cylinder subjected to mechanical shock loading. The governing equation of motion for large deformation problems is derived using meshless local Petrov-Galerkin (MLPG) method based on total lagrangian approach. In the MLPG method, the radial point interpolation technique is employed to construct the shape functions. A micromechanical model based on the Halpin-Tsai model and rule of mixture is used for formulation the nonlinear functionally graded distribution of GPLs in polymer matrix of composites. Energy dissipation in analyses of the structure responding to dynamic loads is considered using the Rayleigh damping. The Newmark-Newton/Raphson method which is an incremental-iterative approach is implemented to solve the nonlinear dynamic equations. The results of the proposed method for homogenous material are compared with the finite element ones. A very good agreement is achieved between the MLPG and FEM with very fine meshing. In addition, the results have demonstrated that the MLPG method is more effective method compared with the FEM for very large deformation problems due to avoiding mesh distortion issues. Finally, the effect of GPLs distribution on strength, stiffness and dynamic characteristics of the cylinder are discussed in details. The obtained results show that the distribution of GPLs changed the mechanical properties, so a classification of different types and volume fraction exponent is established. Indeed by comparing the obtained results, the best compromise of nanocomposite cylinder is determined in terms of mechanical and dynamic properties for different load patterns. All these applications have shown that the present MLPG method is very effective for geometrically nonlinear analyses of GPLR-FG nanocomposite cylinder because of vanishing mesh distortion issue in large deformation problems. In addition, since in proposed method the distributed nodes are used for discretization the problem domain (rather than the meshing), modeling the functionally graded media yields to more accurate results.

Keywords: functionally graded materials; meshless local Petrov-Galerkin method; shock loading; geometrically nonlinear analysis; graphene platelets reinforced nanocomposite

1. Introduction

In functionally graded materials, the material properties varies continuously through one or two directions to achieve the desirable properties such as mechanical properties (Gupta 2007, Rad *et al.* 2015a and Khayat *et al.* 2017), thermal management (Hasselman and Youngblood 1978, Lee *et al.* 1996, Kawasaki and Watanabe 2002 and Bouguenina *et al.* 2015), surface corrosion protection (Schulz *et al.* 2003 and Ocylok *et al.* 2010) and piezoelectric properties (Li and Weng 2002, Shi and Chen 2004 and Xu *et al.* 2018). The most important advantage of the FGMs in compared with the laminated materials is the elimination of stress concentration and delamination due to gradually change in material properties. An extensive overview of the existing literature on stability, buckling, and free vibration analysis of FGMs can be found in Zhang *et al.* (2019) article.

Since in common finite element methods (FEMs), the material properties within each element are assumed to be constant, analysis of FGMs using FEM is encountered with some difficulties (Sladek *et al.* 2005). Thus in recent years, several meshless methods have been developed for analysis of structures made of FGMs to avoid mesh related problems. Zue and Liu (2011) using the local Kriging meshless method studied on functionally graded plates made of a ceramic and metal mixture in which the volume fraction of the ceramic consistent changes continuously through the thickness direction. Sladek *et al.* (2013) proposed a meshless method based on the local Petrov-Galerkin approach for bending analysis of FGM piezoelectric plates. Hosseini *et al.* (2015) worked on transient dynamic analysis of non-Fick diffusion-

∗Corresponding author, Assistant Professor
E-mail: hosein_ghadiri@qiet.ac.ir
[a]Professor
E-mail: shahabf@um.ac.ir
[b]Professor
E-mail: sm_hosseini@um.ac.ir

ISSN: 1229-9367 (Print), 1598-6233 (Online)

elastodynamics problems in functionally graded materials using the MLPG method. The state space differential reproducing kernel (DRK) method was successfully developed for three dimensional analysis of FGM axisymmetric circular plates by Wu and Liu (2016). The static, dynamic and buckling analyses of FG isotropic and sandwich plates using the moving Kriging-based meshfree method with a higher order deformation theory was carried out by Thai *et al.* (2016). A three dimensional meshfree method solution for analysis of functionally graded fiber reinforced cylindrical panels was proposed by Soltanimaleki *et al.* (2016). Chu *et al.* (2016) studied buckling of FG thin plates with in-plane material inhomogeneity using a radial basis function associated with collocation method. The MLPG method was developed by Ferezghi *et al.* (2018) for dynamic analysis of non-symmetric FG cylindrical shell with nonlinear volume fractions through radial direction under mechanical shock loading. Thai *et al*. (2018a) proposed a novel formulation based on an improved moving Kriging meshfree method with naturally stabilized nodal integration for analysis of functionally graded material sandwich plates. Free vibration analysis of FG beams with the open edged cracks using the meshfree boundary domain integral equation method was carried out by Kou and Yang (2019). They presented a comprehensive parameter study of the crack properties, beam material gradient, gradation direction and boundary conditions. Bui *et al.* (2018) developed a meshfree method for analysis of two dimensional fracture problems of cracked FGMs.

One of the most attractive aspects of FGMs is application of theme as the heat shielding materials (Tutuncu and Ozturk 2001). There are several works on analysis of FGMs under thermo-mechanical loadings using the different methods. Wang and Qin (2008) using the method of fundamental solutions coupling with radial basis functions showed that using appropriate graded parameters of FG materials can leads to low stress concentration on structures subjected to mechanical and thermal loads. Krahulec *et al.* (2016) presented a meshless method for time fractional derivative heat conduction in functionally graded materials. A numerical formulation based on the MLPG method was developed by Vaghefi *et al.* (2016) for thermo-elastoplastic analysis of thick FG plates subjected to combined thermal and mechanical loads.

In large deformation problems in which the relationship between the strains and displacements of the structure is nonlinear, the geometrically nonlinear analysis must be taken into account. Some researches have proved that the meshless methods are efficient technique for large deformation problems due to their advantage in eliminating mesh distortion issue (Chen *et al.* 1997, Gu *et al.* 2007 and Rad *et al.* 2015b). There are a large number of research works on geometrically nonlinear analysis of FGMs using meshless methods in the literature. Liu *et al.* (2002) presented the Smooth Particle Hydrodynamics equations governing the elastic and elasto-plastic large deformation dynamic response of solid structures. The geometrically nonlinear analysis of FG thick hollow cylinder with nonlinear grading patterns through radial direction using meshless local Petrov-Galerkin method was carried out by Rad *et al.* (2015c). The geometrically nonlinear analysis of carbon nanotubes reinforced functionally graded composite laminated plates was presented in (Lei *et al.* 2017). A comparative study of geometrical linear and nonlinear bending deformation of functionally graded beams with variable thickness was performed by Lin *et al.* (2018) using the SPH method. A novel plate formulation based on refined plate theory and improved moving Kriging meshfree method was presented by Nguyen *et al.* (2018) for geometric nonlinear static and dynamic analyses of FGM plates. Rad *et al.* (2019) developed the element free Galerkin method for geometrically nonlinear analysis of deep beams considering small scale effect.

Carbon nanotubes reinforced functionally graded materials (CNTR-FG) are the special case of FGMs in which the CNTs are distributed in a matrix of composite material in order to improve its properties. A large number of studies have been conducted to analyze the CNTR-FG composite structures behavior. Ghayoumizadeh *et al.* (2013) developed a formulation based on MLPG method in Laplace-transform domain for 2D elastic wave propagation analysis of functionally graded nanocomposites reinforced by carbon nanotubes. Free vibration of a double walled carbon nanotube beams under axial force was studied by Hajnayeb and Khadem (2015) utilizing Euler-Bernoulli beam theory. Lei *et al.* (2016) presented the buckling analysis of CNTR-FG composite laminated plates of moderate thickness. Arefi *et al.* (2018) focused on analysis of FG-CNTRC cylindrical pressure vessels with different patterns of reinforcement subjected to an inner and outer pressure under a temperature increase. Thai *et al*. (2018b) studied on analysis of carbon nanotube-reinforced composite (CNTRC) plates using the naturally stabilized nodal integration (NSNI) meshfree formulations associated with the higher-order shear deformation plate theory. Mohammadimehr *et al.* (2019) analyzed the magneto-electro-elastic vibration of a FG-CNTRC cylindrical shell resting on viscoelastic foundation. The significant effects of CNTs distribution and orientation on the post buckling behavior of CNTR-FG panels and cylindrical shells are studied by Nguyen *et al.* (2019). A good review of research activities related to functionally graded carbon nanotube reinforced composites is mentioned in Liew *et al.* (2015)article.

Graphene platelets are another kind of reinforcement nanofiller in composites with higher mechanical strength, elastic modulus, specific surface area and lower manufacturing cost compared to CNTs (Verma *et al.* 2014, Yang *et al.* 2017 and Mirzaei and Kiani 2017). Recently, some research have been carried out to investigate the mechanical characteristics of GPLs-reinforced structures. For instance, Feng *et al.* (2017) studied nonlinear free vibration of multi-layer GPL/Polymer nanocomposite beam with four GPL distribution patterns. Buckling and free vibration behavior of initially stressed multilayer Graphene platelets reinforced functionally graded composites (GPLRC_FG) cylindrical shells were studied by Liu *et al.* (2018). Hosseini and Zhang (2018) using the generalized finite difference method proposed a modified

micromechanical model for elastic wave propagation analysis in the GPLs-reinforced nanocomposite cylinder. Thai *et al*. (2019a) focused on dynamic and buckling analysis of GPLRC-FG plates based on four variable refined plate theory and using the NURBS formulation. In another works, they applied NURBS formulation for analysis of multilayer functionally graded GPLRC microplates considering small scale effects based on modified strain gradient theory (Thai *et al*. 2019b) and modified couple stress theory (Thai *et al*. 2019c). In past few years, some researchers have focused on reinforcing the porous material using graphene platelets to achieve more controllable and more specific problem targeting mechanical properties (Kitipornchai *et al.* 2017, Chen *et al.* 2017, Sahmani *et al.* 2018 and Li *et al.* 2018).

To the best of the authors' knowledge, the geometrical nonlinearity has not been considered for GPLs reinforced functionally graded materials with nonlinear grading pattern of GPLs distributions. In this paper for the first time, the MLPG method which is an effective method for large deformation problems is developed for geometrically nonlinear analysis of GPLR-FG nanocomposite cylinders. It should be mentioned that the MLPG method is based on a set of scattered nodes instead of meshes which enables it to easily modeling the functionally graded material and eliminate mesh distortion issue. In addition in MLPG method, the differentiation on the stresses in equilibrium equation is transferred to the weight functions. Thus in this method, the derivatives of stresses and functionally graded distribution of GPLs are not required. The purpose of this paper is to show the mechanical and dynamical properties of GPLR-FG nanocomposite cylinders. For this purpose, various grading pattern of graphene platelets are analyzed using the geometrically nonlinear meshless method to study the effect of adding the graphene platelets on dynamic properties of reinforced nanocomposite cylinder.

2. Radial point interpolations for the variations field

In meshless methods, an arbitrary variation field function u in the vicinity of a point of interest can be approximated using a small number of nodes located in point support domain.

$$u = \mathbf{\Phi}\,\mathbf{U} \tag{1}$$

where $\mathbf{U}$ is the fictions nodal variation field vector and $\mathbf{\Phi}$ is the matrix of shape functions given by

$$\mathbf{\Phi} = \mathbf{R}^{\mathrm{T}}\,\mathbf{R}_{\mathrm{Q}}^{-1} \tag{2}$$

where $\mathbf{R}$ is the vector of radial basis function and $\mathbf{R}_{\mathrm{Q}}$ is the moment matrix of radial basis function which is consists of nodal values of radial basis function vector.

$$\mathbf{R}^{\mathrm{T}} = \begin{bmatrix} R_1(r) & R_2(r) & \ldots & R_n(r) \end{bmatrix} \tag{3}$$

$$\mathbf{R}_{\mathrm{Q}} = \begin{bmatrix} R_1(r_1) & R_2(r_1) & \cdots & R_n(r_1) \\ R_1(r_2) & R_2(r_2) & \cdots & R_n(r_2) \\ \vdots & \vdots & \ddots & \vdots \\ R_1(r_n) & R_2(r_n) & \cdots & R_n(r_n) \end{bmatrix} \tag{4}$$

More details about the radial point interpolation method as well as the various radial basis functions can be found in a previous work of the authors (Rad *et al.* 2015a). In this paper the multi-quadric (MQ) radial basis function is adopted which is given by

$$R_i(r) = \left(r_i^2 + c^2\right)^q \tag{5}$$

in which $q = 1.03$ represents the dimensionless shape parameter which is determined using numerical investigation, c is the average nodal distance in the support domain and r_i is the distance between the point of interest and nodes located in support domain.

3. Functionally graded graphene platelets reinforced cylinder

A cylinder is illustrated with the finite length L, inner radius r_{in} and outer radius r_{out} as shown in Fig. 1. The thick hollow cylinder is reinforced by functionally graded distribution of GPLs along the radial direction. The effective Young's modulus E vary through the radial direction considering the Halpin-Tsai micromechanical model accordingly to following equation (Yang *et al.* 2017).

$$E(r) = \frac{3}{8}E_L + \frac{5}{8}E_T \tag{6}$$

where E_L and E_T represent the longitudinal and transverse moduli of unidirectional lamina, respectively. These parameters in Halpin-Tsai model are defined as (Yang *et al.* 2017)

$$E_L = \frac{1+\xi_L\,\eta_L\,V_{GPL}}{1-\eta_L\,V_{GPL}}E_m \tag{7}$$

$$E_T = \frac{1+\xi_T\,\eta_T\,V_{GPL}}{1-\eta_T\,V_{GPL}}E_m \tag{8}$$

In the last equation V_{GPL} stands for GPLs volume fraction. The length, width, thickness, mass density and elasticity modulus of the GPLs are denoted by a_{GPL}, b_{GPL}, t_{GPL}, ρ_{GPL} and E_{GPL}, respectively. The other parameters of Eqs. (7) and (8) are given by (Yang *et al.* 2017).

$$\xi_L = 2\left(a_{GPL}/t_{GPL}\right) \tag{9}$$

$$\xi_T = 2\left(b_{GPL}/t_{GPL}\right) \tag{10}$$

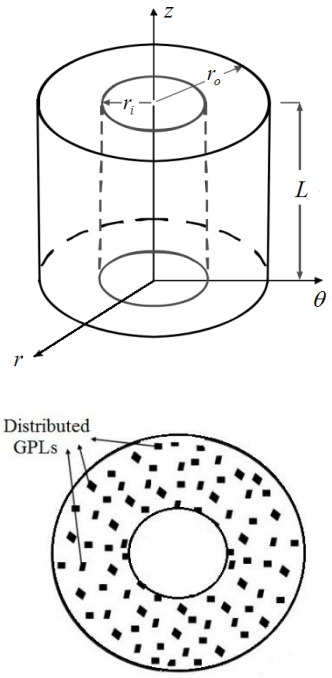

Fig. 1 Studied FG-GPLs reinforced thick hollow cylinder

$$\eta_L = \frac{E_{GPL}/E_m - 1}{E_{GPL}/E_m + \xi_L} \tag{11}$$

$$\eta_T = \frac{E_{GPL}/E_m - 1}{E_{GPL}/E_m + \xi_T} \tag{12}$$

where E_m is the elasticity modulus of polymer matrix. The choice of distribution pattern of graphene platelets in a composite structure is governed by the achievement of interesting mechanical performances. In this paper three possible laws for volume fraction V_{GPL} proposed by Hosseini and Zhang (2018) is considered as follows.

Type 1

$$V_{GPL} = 2V_{GPL}^{*}\left(\frac{r - r_{in}}{r_{out} - r_{in}}\right)^{n} \tag{13}$$

Type 2

$$V_{GPL} = 2V_{GPL}^{*}\left(\frac{r_{out} - r}{r_{out} - r_{in}}\right)^{n} \tag{14}$$

Type 3

$$V_{GPL} = 4HV_{GPL}^{*}\left(\frac{r - r_m}{r_{out} - r_{in}}\right)^{n} \tag{15}$$

Where

$$V_{GPL}^{*} = \frac{W_{GPL}}{W_{GPL} + (\rho_{GPL}/\rho_m)(1 - W_{GPL})} \tag{16}$$

Table 1 Type and volume fraction exponent of different FG-GPLs

FG-GPL	Type	Volume fraction exponent
T1N0.5	1	0.5
T1N1.0	1	1.0
T1N2.0	1	2.0
T1N5.0	1	5.0
T2N0.5	2	0.5
T2N1.0	2	1.0
T2N2.0	2	2.0
T2N5.0	2	5.0
T3N0.5	3	0.5
T3N1.0	3	1.0
T3N2.0	3	2.0
T3N5.0	3	5.0

$$H = \frac{1}{0.5^{(n-1)}} \tag{17}$$

in which, n is the volume fraction exponent, ρ_m is the mass density of polymer matrix and W_{GPL} is the GPL weight fraction. The three nonlinear grading pattern law for $W_{GPL} = 0.3\%$, $r_{in} = 0.5\text{m}$, $r_{out} = 1\text{m}$ and various volume fraction exponent are presented in Fig. 2. In this paper 8 types of FG graphene platelets with different grading pattern namely T1N0.2 to T3N5.0 are studied. The specifications of these materials are summarized in Table 1.

Using the rule of mixture, the mass density $\rho(r)$ and poisson's ratio $\nu(r)$ variation through the radial direction for FG-GPLs reinforced thick hollow cylinder can be expressed by

$$\rho(r) = V_{GPL}\,\rho_{GPL} + V_m\,\rho_m \tag{18}$$

$$\nu(r) = V_{GPL}\,\nu_{GPL} + V_m\,\nu_m \tag{19}$$

It should be mentioned that in Galerkin method, the differentiation on the stresses is transferred to the weight function. Thus in this method, the derivatives of volume fraction V_{GPL} are not required.

4. Kinematics and deformation

As can be seen in Fig. 3, the coordinates of the material points of a body are given by the vector $\mathbf{X}$ in the fixed reference configuration Ω_0 . After the structure is deformed, the position of the material points can be described by their position vector $\mathbf{x}$ at the current deformed configuration Ω .

A differential line in the reference configuration may be mapped into one in the current configuration using the deformation gradient tensor $\mathbf{F}$ (Zienkiewicz and Taylor 2005).

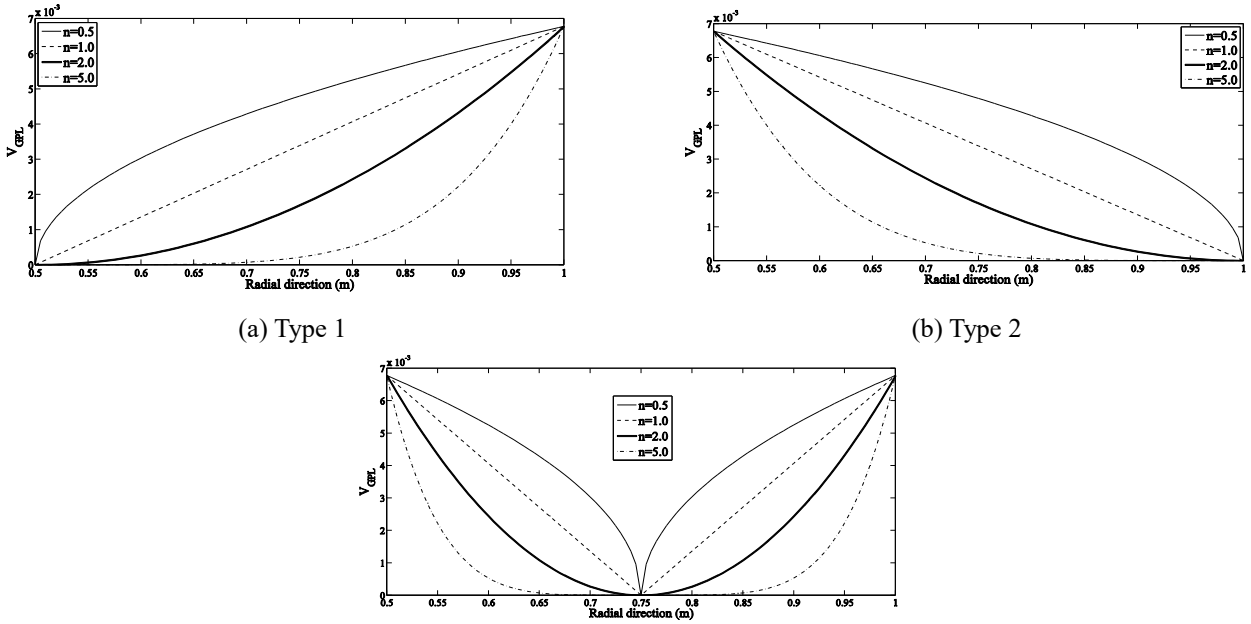

(a) Type 1

(b) Type 2

(c) Type 3

Fig. 2 The adopted GPLs for various types of dispersion patterns

$$\mathrm{d}\,\mathbf{x} = \mathbf{F}\,\mathrm{d}\,\mathbf{X} \tag{20}$$

For axisymmetric problem, where the coordinates are taken as (R,Θ,Z) and (r,θ,z) in the reference and current configurations, the deformation gradient components are given by (Celigoj 2001)

$$\mathbf{F} = \begin{bmatrix} F_{rr} & 0 & F_{rz} \\ 0 & F_{\theta\theta} & 0 \\ F_{zr} & 0 & F_{zz} \end{bmatrix} = \begin{bmatrix} 1+u_{r,R} & 0 & u_{r,Z} \\ 0 & 1+\dfrac{u_r}{R} & 0 \\ u_{z,R} & 0 & 1+u_{z,Z} \end{bmatrix} \tag{21}$$

At the initial state, the deformation gradient matrix is the unit matrix. The increment of deformation gradient components at each load step may be expressed in terms of the incremental nodal displacement, using Eqs. (1) and (21).

$$\Delta\overline{\mathbf{F}} = \mathbf{B}^{\mathrm{l}}\,\Delta\mathbf{U} \tag{22}$$

where $\overline{\mathbf{F}}$ is the deformation gradient vector, $\mathbf{B}^{\mathrm{l}}$ is called the linear strain matrix and $\mathbf{U}$ is the nodal displacement vector.

$$\overline{\mathbf{F}}^{\mathrm{T}} = \{F_{rr} \quad F_{\theta\theta} \quad F_{zz} \quad F_{rz} \quad F_{zr}\} \tag{23}$$

$$\mathbf{B}^{\mathrm{l}} = \left[\mathbf{B}_1^{\mathrm{l}} \quad \mathbf{B}_2^{\mathrm{l}} \quad \cdots \quad \mathbf{B}_n^{\mathrm{l}}\right],\ \mathbf{B}_i^{\mathrm{l}} = \begin{bmatrix} \Phi_{i,r} & 0 \\ \Phi_i / r & 0 \\ 0 & \Phi_{i,z} \\ \Phi_{i,z} & 0 \\ 0 & \Phi_{i,r} \end{bmatrix} \tag{24}$$

$$\mathbf{U}^{\mathrm{T}} = \{u_{r1} \quad u_{z1} \quad u_{r2} \quad u_{z2} \quad \cdots \quad u_{rn} \quad u_{zn}\} \tag{25}$$

The deformation gradient tensor is a fundamental measure of deformations. With the help of the deformation gradient tensor, the Green's strains can be defined as follow.

$$\boldsymbol{\varepsilon} = \frac{1}{2}\left(\mathbf{F}^{\mathrm{T}}\,\mathbf{F} - \mathbf{I}\right) \tag{26}$$

where $\mathbf{I}$ is the unit matrix. The incremental Green's strain components can be computed using the chain rule as

$$\boldsymbol{\Delta\varepsilon} = \frac{1}{2}\left(\mathbf{F}^{\mathrm{T}}\,\boldsymbol{\Delta F} + \boldsymbol{\Delta F}^{\mathrm{T}}\,\mathbf{F}\right) \tag{27}$$

Expanding the terms in the last equation, gives the variation of Green's strain components in terms of the incremental deformation gradient.

$$\Delta\varepsilon_{rr} = F_{rr}\,\Delta F_{rr} + F_{zr}\,\Delta F_{zr} \tag{28}$$

$$\Delta\varepsilon_{\theta\theta} = F_{\theta\theta}\,\Delta F_{\theta\theta} \tag{29}$$

$$\Delta\varepsilon_{zz} = F_{zz}\,\Delta F_{zz} + F_{rz}\,\Delta F_{rz} \tag{30}$$

$$\begin{aligned} \Delta\gamma_{rz} &= \Delta\varepsilon_{rz} + \Delta\varepsilon_{zr} = \\ &F_{rz}\,\Delta F_{rr} + F_{zr}\,\Delta F_{zz} + F_{rr}\,\Delta F_{rz} + F_{zz}\,\Delta F_{zr} \end{aligned} \tag{31}$$

The Eqs. (28) to (31) can be written in matrix form as

$$\boldsymbol{\Delta\varepsilon} = \hat{\mathbf{F}}\,\Delta\overline{\mathbf{F}} \tag{32}$$

where

$$\hat{\mathbf{F}} = \begin{bmatrix} F_{rr} & 0 & 0 & 0 & F_{zr} \\ 0 & F_{\theta\theta} & 0 & 0 & 0 \\ 0 & 0 & F_{zz} & F_{rz} & 0 \\ F_{rz} & 0 & F_{zr} & F_{rr} & F_{zz} \end{bmatrix} \tag{33}$$

The variation of Green's strains may now be written with respect to the increment of nodal displacement by substituting Eq. (22) into Eq. (32) to obtain

$$\Delta\bar{\boldsymbol{\varepsilon}} = \left(\hat{\mathbf{F}}\ \mathbf{B}^{\mathrm{l}}\right)\Delta\mathbf{U} = \mathbf{B}^{\mathrm{nl}}\,\Delta\mathbf{U} \tag{34}$$

where $\mathbf{B}^{\mathrm{nl}}$ is called the nonlinear strain matrix and defined as

$$\mathbf{B}_i^{\mathrm{nl}} = \begin{bmatrix} F_{rr}\,\boldsymbol{\Phi}_{i,r} & F_{zr}\,\boldsymbol{\Phi}_{i,r} \\ F_{\theta\theta}\,\boldsymbol{\Phi}_i / r & 0 \\ F_{rz}\,\boldsymbol{\Phi}_{i,z} & F_{zz}\,\boldsymbol{\Phi}_{i,z} \\ F_{rr}\,\boldsymbol{\Phi}_{i,z} + F_{rz}\,\boldsymbol{\Phi}_{i,r} & F_{zr}\,\boldsymbol{\Phi}_{i,z} + F_{zz}\,\boldsymbol{\Phi}_{i,r} \end{bmatrix} \tag{35}$$

$$\mathbf{B}^{\mathrm{nl}} = \begin{bmatrix} \mathbf{B}_1^{\mathrm{nl}} & \mathbf{B}_2^{\mathrm{nl}} & \cdots & \mathbf{B}_n^{\mathrm{nl}} \end{bmatrix}$$

5. Constitutive model

The Green's strain tensor ε_{ij} is energetically-conjugate to the rate of second Piola-Kirchhoff stress tensor S_{ij}, since they produces the energy stored in the deformable medium with respect to the initial configuration (Reddy 2014). In the Lagrangian description in which the motion of a body is referred to a reference configuration, the second Piola-Kirchhoff stress components are related to Green's strain tensor as

$$\Delta\bar{\mathbf{S}} = \mathbf{C}(r)\Delta\bar{\boldsymbol{\varepsilon}} \tag{36}$$

where

$$\bar{\mathbf{S}}^{\mathrm{T}} = \begin{Bmatrix} S_{rr} & S_{\theta\theta} & S_{zz} & S_{rz} & S_{zr} \end{Bmatrix} \tag{37}$$

$$\bar{\boldsymbol{\varepsilon}}^{\mathrm{T}} = \begin{Bmatrix} \varepsilon_{rr} & \varepsilon_{\theta\theta} & \varepsilon_{zz} & \varepsilon_{rz} & \varepsilon_{zr} \end{Bmatrix} \tag{38}$$

$$\mathbf{C}(r) = \frac{E(r)}{(1+\nu(r))(1-2\nu(r))} \times \begin{bmatrix} 1-\nu(r) & \nu(r) & \nu(r) & 0 & 0 \\ \nu(r) & 1-\nu(r) & \nu(r) & 0 & 0 \\ \nu(r) & \nu(r) & 1-\nu(r) & 0 & 0 \\ 0 & 0 & 0 & \dfrac{1-2\nu(r)}{2} & 0 \\ 0 & 0 & 0 & 0 & \dfrac{1-2\nu(r)}{2} \end{bmatrix} \tag{39}$$

where $E(r)$ and $\nu(r)$ are introduced in Eqs. (6) and (19), respectively. Substitution of Eq. (34) in to Eq. (36) results in the variation of second Piola-Kirchhoff stress in terms of the increment of nodal displacement.

$$\Delta\bar{\mathbf{S}} = \mathbf{C}(r)\mathbf{B}^{\mathrm{nl}}\,\Delta\mathbf{U} \tag{40}$$

6. Geometrically nonlinear Meshless local Perov-Galerkin Method

Using quantities related to the current (deformed) configuration, the governing equilibrium equation of motion for axisymmetric problems in cylindrical coordinates can be expressed as

$$\sigma_{rr,r} + \sigma_{zr,z} + \frac{\sigma_{rr} - \sigma_{\theta\theta}}{r} - \rho\,\ddot{u}_r = 0 \tag{41}$$

$$\sigma_{zz,z} + \sigma_{rz,r} + \frac{\sigma_{rz}}{r} - \rho\,\ddot{u}_z = 0 \tag{42}$$

where σ is the Cauchy (true) stress and ρ is the mass density in the current configuration. Using the weight function W, the Galerkin weak form of Eqs. (41) and (42) in a local subdomain at the current configuration Ω can be written as

$$\int_{\Omega}\left(\sigma_{rr,r} + \sigma_{zr,z} + \frac{\sigma_{rr} - \sigma_{\theta\theta}}{r} - \rho\,\ddot{u}_r\right) rW\,\mathrm{d}\Omega = 0 \tag{43}$$

$$\int_{\Omega}\left(\sigma_{zz,z} + \sigma_{rz,r} + \frac{\sigma_{rz}}{r} - \rho\,\ddot{u}_z\right) rW\,\mathrm{d}\Omega = 0 \tag{44}$$

Applying the Green divergence theorem and using the chain rule, Eqs. (43) and (44) can be written as

$$\begin{aligned} &-\int_{\Gamma_i+\Gamma_u}\left(\sigma_{rr}n_r + \sigma_{zr}n_z\right) rW\,\mathrm{d}\Gamma + \\ &\int_{\Omega}\left(r\sigma_{rr}\,W_{,r} + r\sigma_{zr}\,W_{,z} + \sigma_{\theta\theta}\,W\right)\mathrm{d}\Omega + \\ &\int_{\Omega}\left(\rho\,\ddot{u}_r\right) rW\,\mathrm{d}\Omega = \int_{\Gamma_t}\left(\sigma_{rr}n_r + \sigma_{zr}n_z\right) rW\,\mathrm{d}\Gamma \end{aligned} \tag{45}$$

$$\begin{aligned} &-\int_{\Gamma_i+\Gamma_u}\left(\sigma_{zz}n_z + \sigma_{rz}n_r\right) rW\,\mathrm{d}\Gamma + \\ &\int_{\Omega}\left(r\sigma_{rz}\,W_{,r} + r\sigma_{zz}\,W_{,z}\right)\mathrm{d}\Omega \\ &+\int_{\Omega}\left(\rho\,\ddot{u}_z\right) rW\,\mathrm{d}\Omega = \int_{\Gamma_t}\left(\sigma_{zz}n_z + \sigma_{rz}n_r\right) rW\,\mathrm{d}\Gamma \end{aligned} \tag{46}$$

As shown in Fig. 4, Γ is the boundary of subdomain Ω, which is composed of three parts including interior boundary Γ_i, essential (displacement) boundary Γ_u and natural (force or free) boundary Γ_t. Expressed in matrix form, Eqs. (45) and (46) becomes

$$\begin{aligned} &\int_{\Omega}\mathbf{W}'\,\bar{\boldsymbol{\sigma}}\,\mathrm{d}\Omega - \int_{\Gamma_i+\Gamma_u} r\,\mathbf{W}\mathbf{N}\bar{\boldsymbol{\sigma}}\,\mathrm{d}\Gamma + \\ &\int_{\Omega} r\,\rho\,\mathbf{W}\ddot{\bar{\mathbf{u}}}\,\mathrm{d}\Omega = \int_{\Gamma_t} r\,\mathbf{W}\bar{\mathbf{T}}\,\mathrm{d}\Gamma \end{aligned} \tag{47}$$

where

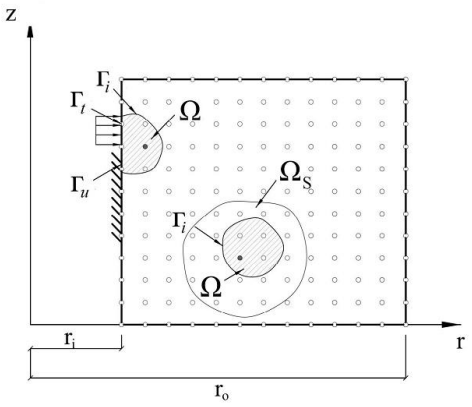

Fig. 4 Local subdomains and parts of boundaries for axisymmetric problems

$$\mathbf{W}' = \begin{bmatrix} rW_{,r} & W & 0 & 0 & rW_{,z} \\ 0 & 0 & rW_{,z} & rW_{,r} & 0 \end{bmatrix} \tag{48}$$

$$\bar{\boldsymbol{\sigma}}^{\mathrm{T}} = \{\sigma_{rr} \quad \sigma_{\theta\theta} \quad \sigma_{zz} \quad \sigma_{rz} \quad \sigma_{zr}\} \tag{49}$$

$$\mathbf{W} = \begin{bmatrix} W & 0 \\ 0 & W \end{bmatrix} \tag{50}$$

$$\mathbf{N} = \begin{bmatrix} n_r & 0 & 0 & 0 & n_z \\ 0 & 0 & n_z & n_r & 0 \end{bmatrix} \tag{51}$$

$$\bar{\mathbf{u}}^{\mathrm{T}} = \{u_r \quad u_z\},\ \bar{\ddot{\mathbf{u}}}^{\mathrm{T}} = \{\ddot{u}_r \quad \ddot{u}_z\},\ \bar{\mathbf{T}}^{\mathrm{T}} = \{t_r \quad t_z\} \tag{52}$$

The equilibrium equation of motion may also be written for the reference configuration using the following relations between stress measures (Reddy 2014).

$$\boldsymbol{\sigma} = \frac{1}{J}\mathbf{F}\mathbf{S}\mathbf{F}^{\mathrm{T}} \tag{53}$$

where $\mathbf{F}$ is the deformation gradient matrix, J is the determinant of $\mathbf{F}$ and $\mathbf{S}$ is the second Piola-Kirchhoff stress matrix.

$$\boldsymbol{\sigma} = \begin{bmatrix} \sigma_{rr} & \sigma_{r\theta} & \sigma_{rz} \\ \sigma_{\theta r} & \sigma_{\theta\theta} & \sigma_{\theta z} \\ \sigma_{zr} & \sigma_{z\theta} & \sigma_{zz} \end{bmatrix}, \mathbf{S} = \begin{bmatrix} S_{rr} & S_{r\theta} & S_{rz} \\ S_{\theta r} & S_{\theta\theta} & S_{\theta z} \\ S_{zr} & S_{z\theta} & S_{zz} \end{bmatrix} \tag{54}$$

The mass density, local subdomain, boundary of subdomain and unit normal vector (direction cosines) at the initial configuration are related to their values at the current configuration through the following mappings.

$$\rho = \frac{\rho_0}{J},\ \mathrm{d}\Omega = J\,\mathrm{d}\Omega_0\ ,\ \mathrm{d}\Gamma = J\,\mathrm{d}\Gamma_0 \tag{55}$$

$$\mathbf{N} = \mathbf{F}^{-\mathrm{T}}\mathbf{N}_0 \tag{56}$$

Substituting Eqs. (53), (55) and (56) into Eq. (47) leads to equation of motion with respect to the initial configuration.

$$\begin{aligned} &\int_{\Omega_0} \mathbf{W}'\hat{\mathbf{F}}\,\bar{\mathbf{S}}\,\mathrm{d}\Omega - \int_{\Gamma_{i0}+\Gamma_{u0}} r\mathbf{W}\mathbf{N}_0\,\hat{\mathbf{F}}\bar{\mathbf{S}}\,\mathrm{d}\Gamma + \\ &\int_{\Omega_0} r\rho_0\,\mathbf{W}\bar{\ddot{\mathbf{u}}}\,\mathrm{d}\Omega = \int_{\Gamma_{t0}} r\mathbf{W}\bar{\mathbf{T}}\,\mathrm{d}\Gamma \end{aligned} \tag{57}$$

It should be mentioned that the last equation is nonlinear because the both sides of this equation are function of nodal displacement. Thus, an incremental-iterative setting must be established that obtains a solution for a time step $t+\mathrm{d}t$ given the state at time step t. The incremental form of Eq. (57) may be obtained using the chain rule given by

$$\Delta\left(\hat{\mathbf{F}}\bar{\mathbf{S}}\right) = \hat{\mathbf{F}}\Delta\left(\bar{\mathbf{S}}\right) + \hat{\mathbf{S}}\Delta\left(\bar{\mathbf{F}}\right) \tag{58}$$

where

$$\hat{\mathbf{S}} = \begin{bmatrix} S_{rr} & 0 & 0 & S_{rz} & 0 \\ 0 & S_{\theta\theta} & 0 & 0 & 0 \\ 0 & 0 & S_{zz} & 0 & S_{zr} \\ 0 & 0 & S_{rz} & 0 & S_{rr} \\ S_{zr} & 0 & 0 & S_{zz} & 0 \end{bmatrix} \tag{59}$$

Applying the Eq. (58) into Eq. (57) yields to

$$\begin{aligned} &\int_{\Omega_0} \mathbf{W}'\hat{\mathbf{F}}\,\Delta\bar{\mathbf{S}}\,\mathrm{d}\Omega - \int_{\Gamma_{i0}+\Gamma_{u0}} r\mathbf{W}\mathbf{N}_0\,\hat{\mathbf{F}}\,\Delta\bar{\mathbf{S}}\,\mathrm{d}\Gamma \\ &+ \int_{\Omega_0} \mathbf{W}'\hat{\mathbf{S}}\,\Delta\bar{\mathbf{F}}\,\mathrm{d}\Omega - \int_{\Gamma_{i0}+\Gamma_{u0}} r\mathbf{W}\mathbf{N}_0\,\hat{\mathbf{S}}\,\Delta\bar{\mathbf{F}}\,\mathrm{d}\Gamma + \\ &\int_{\Omega_0} r\rho_0\,\mathbf{W}\Delta\bar{\ddot{\mathbf{u}}}\,\mathrm{d}\Omega = \int_{\Gamma_{t0}} r\mathbf{W}\bar{\mathbf{T}}\,\mathrm{d}\Gamma - \int_{\Omega_0} r\rho_0\,\mathbf{W}\bar{\ddot{\mathbf{u}}}\,\mathrm{d}\Omega - \\ &\int_{\Omega_0} \mathbf{W}'\hat{\mathbf{F}}\,\bar{\mathbf{S}}\,\mathrm{d}\Omega + \int_{\Gamma_{i0}+\Gamma_{u0}} r\mathbf{W}\mathbf{N}_0\,\hat{\mathbf{F}}\,\bar{\mathbf{S}}\,\mathrm{d}\Gamma \end{aligned} \tag{60}$$

Substituting Eqs. (22) and (40) into Eq. (60), the nonlinear incremental equation of motion can be summarized in the following matrix form.

$$\mathbf{M}\Delta\ddot{\mathbf{U}} + \mathbf{C}\Delta\dot{\mathbf{U}} + \mathbf{K}_{\mathrm{T}}\Delta\mathbf{U} = \Delta\mathbf{P} \tag{61}$$

where

$$\mathbf{M} = \int_{{}_0\boldsymbol{\Omega}_{\mathrm{Q}}} r\rho_0\,\mathbf{W}\boldsymbol{\Phi}\,\mathrm{d}\Omega \tag{62}$$

$$\begin{aligned} \mathbf{K}_{\mathrm{T}} = &-\int_{{}_0\boldsymbol{\Gamma}_{\mathrm{Qi}}+{}_0\boldsymbol{\Gamma}_{\mathrm{Qu}}} r\mathbf{W}\mathbf{N}\left(\hat{\mathbf{F}}\mathbf{C}(r)\mathbf{B}^{\mathrm{nl}} + \hat{\mathbf{S}}\mathbf{B}^{\mathrm{l}}\right)\mathrm{d}\Gamma \\ &+ \int_{{}_0\boldsymbol{\Omega}_{\mathrm{Q}}} \mathbf{W}'\left(\hat{\mathbf{F}}\mathbf{C}(r)\mathbf{B}^{\mathrm{nl}} + \hat{\mathbf{S}}\mathbf{B}^{\mathrm{l}}\right)\mathrm{d}\Omega \end{aligned} \tag{63}$$

$$\Delta\mathbf{P}_n = \int_{\Gamma_{t0}} r\,\mathbf{W}\,\overline{\mathbf{T}}\,\mathrm{d}\Gamma + \int_{\Gamma_{i0}+\Gamma_{u0}} r\,\mathbf{W}\,\mathbf{N}_0\left(\hat{\mathbf{F}}\,\overline{\mathbf{S}}\right)\mathrm{d}\Gamma - \int_{\Omega_0} \mathbf{W}'\left(\hat{\mathbf{F}}\,\overline{\mathbf{S}}\right)\mathrm{d}\Omega - \left(\int_{\Omega_0} r\,\rho_0\,\mathbf{W}\,\mathbf{\Phi}\,\mathrm{d}\Omega\right)\ddot{\mathbf{U}} \tag{64}$$

In Eq. (61), $\mathbf{C}$ is the damping matrix. In this paper the damping matrix is constructed using Rayleigh method with respect to the mass and initial stiffness matrices.

$$\mathbf{C} = \alpha\,\mathbf{M} + \beta\,\mathbf{K}_0 \tag{65}$$

where $\mathbf{K}_0$ is the initial stiffness matrix, α and β are constants with s^{-1} and s units, respectively. The α and β parameters can be determined using specified damping ratios ξ_i and ξ_j at the i th and j th modes of vibration.

$$\left(\frac{1}{2}\right)\begin{bmatrix} 1/\omega_i & \omega_i \\ 1/\omega_j & \omega_j \end{bmatrix}\begin{Bmatrix}\alpha \\ \beta\end{Bmatrix} = \begin{Bmatrix}\xi_i \\ \xi_j\end{Bmatrix} \tag{66}$$

In this paper, two first modes of vibration with the same damping ratios are considered for obtaining the damping matrix. To solve the resulting nonlinear equation (Eq. (61)), a standard Newmark/Newton-Raphson solution method has been mentioned which is presented in the next section.

7. Newmark/Newton-Raphson method

In this paper the implicit time integration method (Newmark method) is implemented to discrete the forced vibration equations at time domain and the Newton-Raphson iterative solution scheme is used to linearize the equation at each time steps. The Newmark method states that the first and second derivatives of displacement vectors (velocity and acceleration vectors) at the time step t_{i+1} can be defined with respect to the pervious time step as follows.

$$\ddot{\mathbf{U}}_{i+1} = \frac{1}{\beta(\Delta t)^2}\left(\mathbf{U}_{i+1} - \mathbf{U}_i\right) - \frac{1}{\beta(\Delta t)^2}\dot{\mathbf{U}}_i - \left(\frac{1}{2\beta} - 1\right)\ddot{\mathbf{U}}_i \tag{67}$$

$$\dot{\mathbf{U}}_{i+1} = \dot{\mathbf{U}}_i + \left[(1-\gamma)\Delta t\right]\ddot{\mathbf{U}}_i + \gamma\,\Delta t\,\ddot{\mathbf{U}}_{i+1} \tag{68}$$

In this study, the Newmark parameters is considered as $\beta = 0.25$ and $\gamma = 0.5$, which yields to the constant average acceleration method. Applying Eqs. (67) and (68) into Eq. (61), the nonlinear quasi-static equation of motion can be achieved at each time step.

$$\hat{\mathbf{K}}_{\mathrm{T}}\,\Delta\mathbf{U}_i = \Delta\hat{\mathbf{P}}_i \tag{69}$$

where

$$\hat{\mathbf{K}}_{\mathrm{T}} = \mathbf{K}_{\mathrm{T}} + \frac{1}{\beta(\Delta t)^2}\mathbf{M} + \frac{\gamma}{\beta(\Delta t)}\mathbf{C} \tag{70}$$

$$\Delta\hat{\mathbf{P}}_i = \Delta\mathbf{P}_i + \left(\frac{1}{\beta(\Delta t)^2}\mathbf{M} + \frac{\gamma}{\beta(\Delta t)}\mathbf{C}\right)\dot{\mathbf{U}}_{i-1} + \left(\left(\frac{1}{2\beta} - 1\right)\mathbf{M} + \left(\frac{\gamma}{2\beta} - 1\right)\mathbf{C}\right)\ddot{\mathbf{U}}_{i-1} \tag{71}$$

The solution of the nonlinear quasi static equation of motion at each time steps is obtained through the iterative Newton-Raphson technique as described in our previous published paper (Rad *et al.* 2019).

8. Numerical results and discussions

8.1 Verification

To verify the accuracy of proposed MLPG method at present study, a FGGPLs-reinforced thick hollow cylinder with the following boundary conditions is analyzed and the results are compared with those obtained by FEM.

$$t_r(r_i, z) = 0, \qquad t_z(r_i, z) = 0 \tag{72}$$

$$t_r(r_o, z) = f_n, \qquad t_z(r_o, z) = 0 \tag{73}$$

$$u_r(r, 0) = 0, \qquad u_z(r, 0) = 0 \tag{74}$$

where f_n is the external uniform load applied on outer surface at top of the cylinder in n 'th load step (see Fig. 5).

$$f_n = \begin{cases} n\,P_0 & z = L \\ 0 & z \neq L \end{cases} \tag{75}$$

where $P_0 = 3.5\times10^5\ N/m$. The dimension of the cylinder is $r_i = 0.3m$, $r_o = 0.4m$, and $L = 0.5m$ as the inner radius, outer radius and length of the cylinder, respectively. The properties of the epoxy matrix and graphene platelets are considered as the same reported by Yang *et al.* (2017).

$$E_m = 3GPa,\ \rho_m = 1200\,kg/m^3,\ \nu_m = 0.34 \tag{76}$$

$$\begin{aligned} &E_{GPL} = 1.01TPa,\ \rho_{GPL} = 1062.5\,kg/m^3 \\ &\nu_{GPL} = 0.186,\ a_{GPL} = 2.5\,\mu m,\ b_{GPL} = 1.5\,\mu m \\ &t_{GPL} = 1.5\,nm,\ W_{GPL} = 0.3\% \end{aligned} \tag{77}$$

If the GPL weight fraction W_{GPL} considered to be zero, the thick hollow cylinder becomes an isotropic polymer and it is possible to compare the obtained results with the FEM. In this paper, an axisymmetric four nodes element with two degrees of freedom at each node is used in finite element model. In Table 2, the radial displacements of point 'A' are compared with those obtained using finite element method. According to this table, a good agreement between the

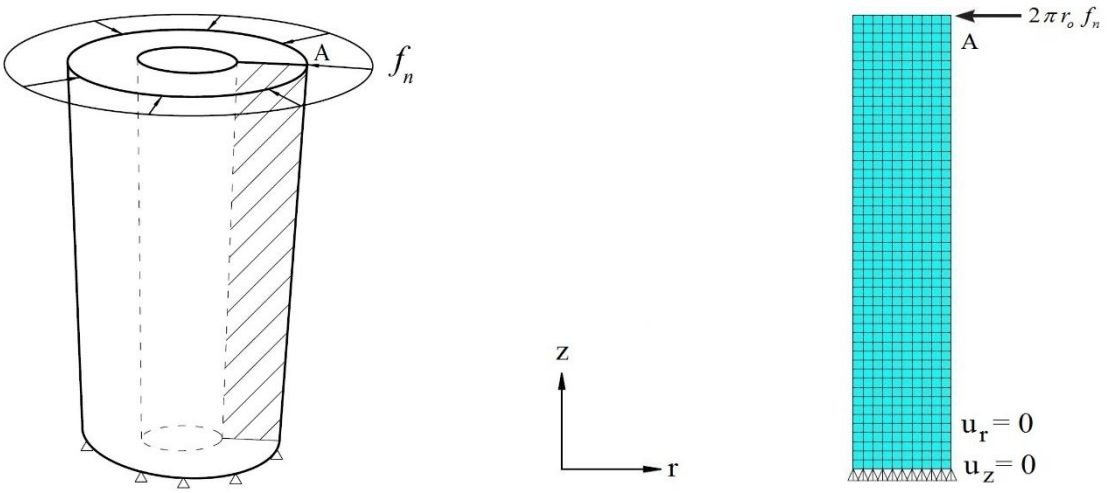

Fig. 5 An axisymmetric thick hollow cylinder and its boundary conditions

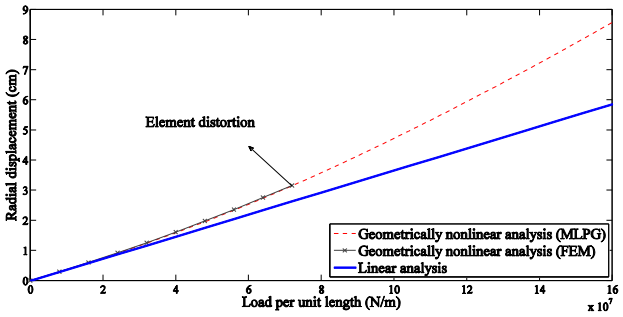

Fig. 6 Comparison between the FEM and MLPG results

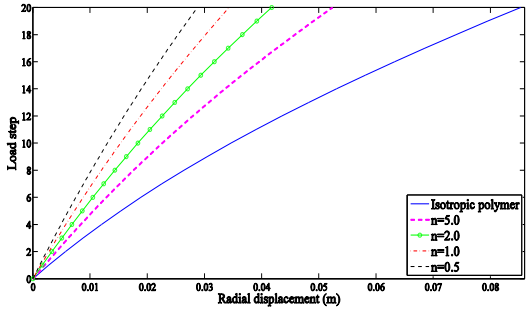

(a) Type 1

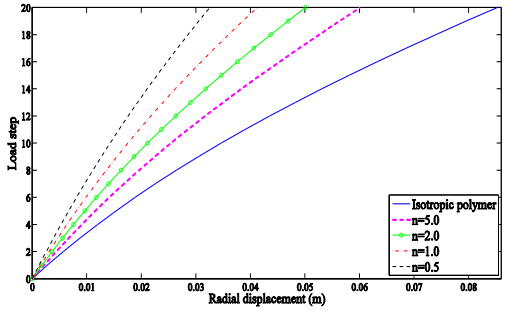

(b) Type 2

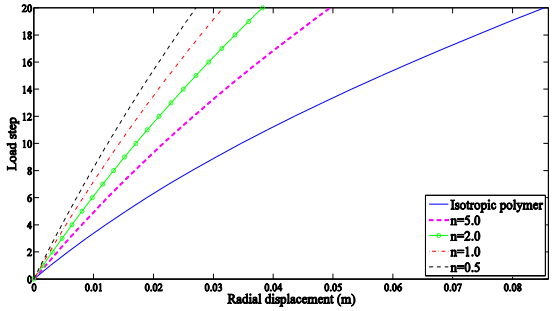

(c) Type 3

Fig. 7 The load step versus nonlinear radial displacement responses at the point ‘A’ for various volume fraction index

Table 2 Radial displacement of pint 'A' obtained by MLPG method compared with reference FEM results (2000 elements with 2021 nodes)

Loading steps (n)		1	2	3	4	5	6	7	8	9
FEM	$-u_r^{\mathrm{A}}(cm)$	0.289	0.591	0.906	1.236	1.583	1.945	2.321	2.711	3.107
MLPG (6×24)	$-u_r^{\mathrm{A}}(cm)$	0.267	0.545	0.834	1.136	1.450	1.777	2.119	2.475	2.847
	dif (%)	7.61	7.78	7.95	8.09	8.40	8.64	8.70	8.71	8.37
MLPG (6×30)	$-u_r^{\mathrm{A}}(cm)$	0.271	0.554	0.848	1.155	1.476	1.810	2.159	2.523	2.902
	dif (%)	6.23	6.26	6.40	6.55	6.76	6.94	6.98	6.93	6.60
MLPG (8×32)	$-u_r^{\mathrm{A}}(cm)$	0.280	0.573	0.879	1.200	1.536	1.888	2.257	2.642	3.045
	dif (%)	3.11	3.05	2.98	2.91	2.97	2.93	2.76	2.55	2.00
MLPG (8×40)	$-u_r^{\mathrm{A}}(cm)$	0.284	0.582	0.894	1.221	1.564	1.924	2.301	2.695	3.105
	dif (%)	1.73	1.52	1.32	1.21	1.20	1.08	0.86	0.59	0.06

results of presented MLPG method (with 8×40 nodal distribution) and finite element method with very fine meshing (2000 elements with 2021 nodes) is achieved at the all load steps.

In this table, the percentage difference of the MLPG method with the FEM is obtained from the following equation.

$$\text{dif }(\%)=\left|\frac{u_r^{FEM}-u_r^{MLPG}}{u_r^{FEM}}\right|\times 100 \tag{78}$$

It should be mentioned that after 9th load step, because of mesh distortion issue, the FEM results become unstable.

Fig. 6 plots the load-displacement diagram obtained by MLPG method for 20 loading steps comparing with the linear and FEM results. According to this figure, it is found that very stable results obtained by the presented geometrically nonlinear MLPG method. In addition, the difference between linear and geometrically nonlinear analyses shows that the effect of large deformation cannot be negligible. So that the geometrically nonlinear analysis makes the cylinder softer than the linear solutions as the load steps increases.

The effect of volume fraction index on stiffness and strength of the cylinder for various types of GPLs dispersion patterns is investigated in Fig. 7. As it can be seen in this figure, the cylinder strength and stiffness decreases with the increase of the volume fraction index for all three types of distributions. In addition, by comparing Figs. 7(a)-7(c) it is obvious that the cylinder stiffness depend on the laws for volume fraction (type of nonlinear grading pattern). For example at the end of load steps, the radial displacement of the T3N0.5 cylinder decreases by about 68.24% compared to isotropic polymer cylinder. In contrast, the T1N0.5 and T2N0.5 has a lower reduction in radial displacement (66.28% and 61.82% lower than isotropic polymer cylinder, respectively).

8.2 Free vibration analysis

For free vibration analysis, the following boundary conditions is assumed for the aforementioned cylinder (see Fig. 8).

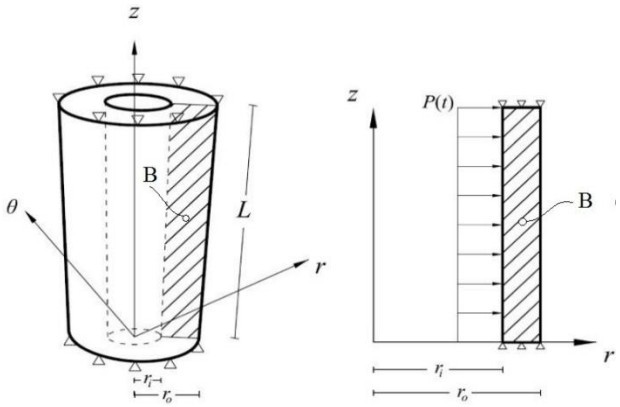

Fig. 8 Thick hollow cylinder under axisymmetric shock loading at the inner surface

$$t_r(r_i,z,t)=P(t),\quad t_z(r_i,z,t)=0 \tag{79}$$

$$t_r(r_o,z,t)=0,\quad t_z(r_o,z,t)=0 \tag{80}$$

$$t_r(r,0,t)=0,\quad t_r(r,L,t)=0 \tag{81}$$

$$u_z(r,0,t)=0,\quad u_z(r,L,t)=0 \tag{82}$$

Table 3 shows the values of the normalized frequencies associated to the first four vibration modes of the cylinders with various grading pattern at the initial state comparing with the isotropic polymer cylinder. The normalized natural frequencies are defined as

$$\varpi_i=\left(L\sqrt{\frac{\rho_m}{E_m}}\right)\times\omega_i \tag{83}$$

According to the considered modes, the frequencies of the cylinder made of T2N0.5 is 51 to 54% higher than those of isotropic polymer ones. The relation between the volume fraction index and the normalized frequencies of mode I and mode II for various types of grading pattern are shown

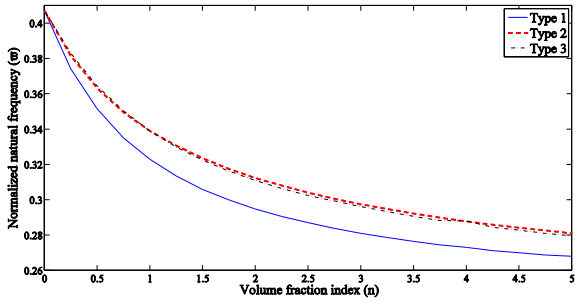

(a) Mode I

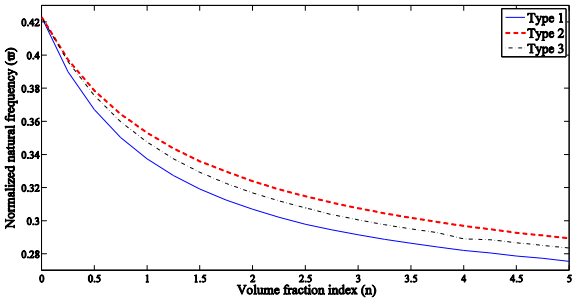

(b) Mode II

Fig. 9 The effect of volume fraction index on initial natural frequencies

Table 3 The normalized natural frequencies ϖ of the thick hollow cylinder with various GPLs distribution patterns compared to isotropic polymer at the initial state

	Isotropic Polymer	Type 1				Type 2				Type 3			
		n=0.5	n=1.0	n=2.0	n=5.0	n=0.5	n=1.0	n=2.0	n=5.0	n=0.5	n=1.0	n=2.0	n=5.0
ϖ_1	0.2338	0.3502	0.3215	0.2925	0.2668	0.3611	0.3371	0.3101	0.2811	0.3606	0.3385	0.3078	0.2762
dif (%)	-	49.79	37.51	25.11	14.11	54.45	44.18	32.63	20.23	54.23	44.78	31.65	18.14
ϖ_2	0.2438	0.3655	0.3364	0.3061	0.2742	0.3772	0.3518	0.3228	0.2854	0.3734	0.3424	0.3152	0.2825
dif (%)	-	49.92	37.98	25.55	12.47	54.72	44.30	32.40	17.06	53.16	40.44	29.29	15.87
ϖ_3	0.3655	0.5423	0.4983	0.4577	0.4204	0.5522	0.5119	0.4730	0.4330	0.5717	0.5342	0.4933	0.4468
dif (%)	-	48.37	36.33	25.23	15.02	51.08	40.05	29.41	18.47	56.42	46.16	34.97	22.24
ϖ_4	0.5318	0.8189	0.7602	0.6947	0.6208	0.8012	0.7364	0.6688	0.6004	0.8123	0.7505	0.6844	0.6129
dif (%)	-	53.99	42.95	30.63	16.74	50.66	38.47	25.76	12.90	52.75	41.12	28.70	15.25

in Figs. 9 (a) and 9 (b), respectively. It can be seen that for larger volume fraction index, the natural frequencies become smaller. It may be explained that the higher volume fraction index, the lower cylinder stiffness and the frequencies hence reduces.

8.3 Dynamic analysis

To continue the analysis, the following radial traction force applied on internal bounding surface of the cylinder is considered for the problem (see Fig. 10).

$$t_r(r_i,z,t)=P(t)=\begin{cases}P_0\,t & t\le t_0\\ 0 & t>t_0\end{cases} \tag{84}$$

where P_0 and t_0 are assumed to be $100\,\text{GPa/s}$ and 0.004s, respectively. The other boundary conditions are the same previously defined in Eqs. (79) to (82).

The time histories of the linear and nonlinear radial displacement for T3N0.5 cylinder at point 'B' (see Fig. 8) is shown in Fig. 11. According to this figure, the large deformations effects on amplitude and period of vibration. In other words for this kind of loading, the geometrically nonlinear analysis causes to smaller amplitude and larger period of vibration compared to linear analysis.

Based on Eq. (79), by increasing the time steps up to the t_0, the applied load and consequently the cylinder deformations will be increased (see Fig. 11).

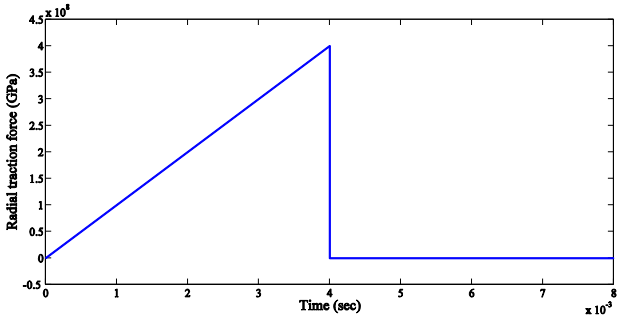

Fig. 10 The radial traction force applied on internal surface of cylinder

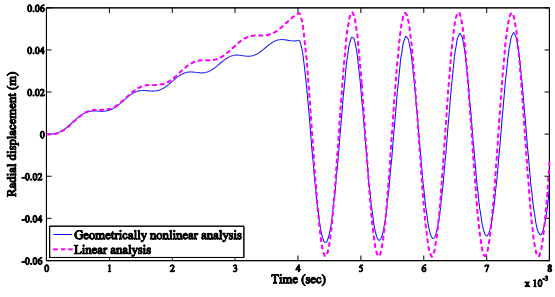

Fig. 11 Comparison between the linear and geometrically nonlinear time histories

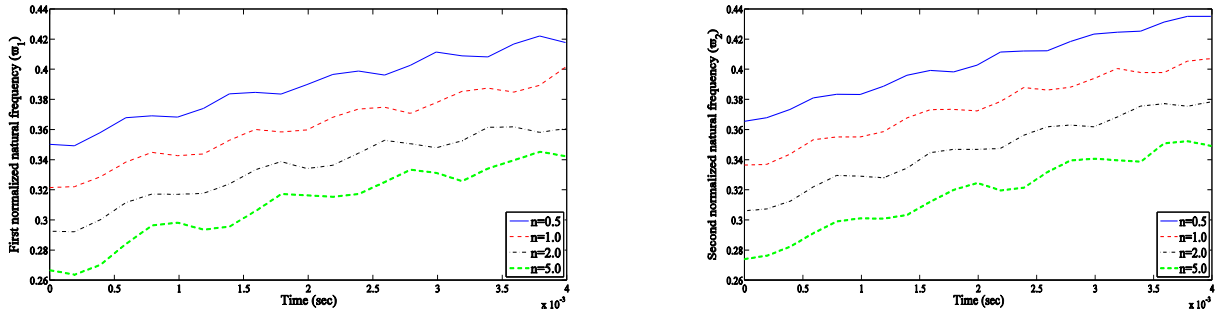

(a) Mode I (b) Mode II

Fig. 12 The effect of large deformations on natural frequencies of the GPLRR-FG cylinder (Type I)

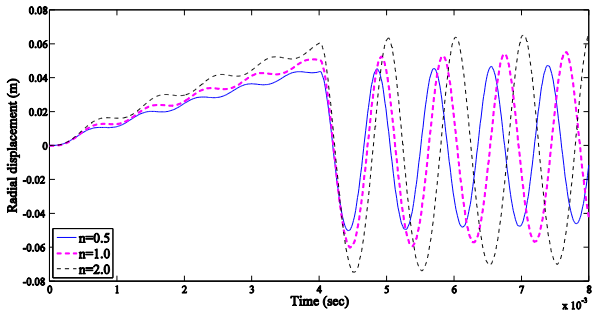

Fig. 13 The radial displacement time history of the cylinder made of T2N0.5, T2N1.0 and T2N2.0

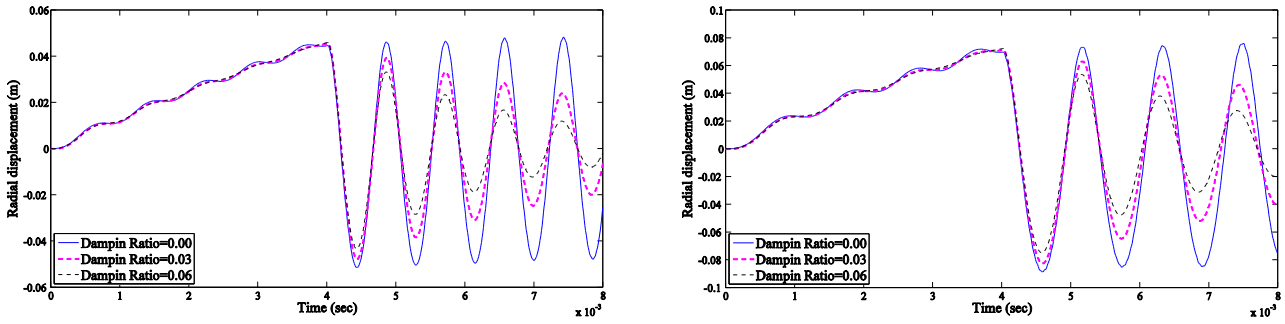

(a) T3N0.5 (b) T3N5.0

Fig. 14 The time history of radial displacement considering Rayleigh damping with various damping ratios

Based on Eq. (79), by increasing the time steps up to the t_0 , the applied load and consequently the cylinder deformations will be increased (see Fig. 11). The results of the higher natural frequencies ϖ_1 and ϖ_2 for various GPLs distributions at four time steps are listed in table 4.

The effect of large deformations on the first and second natural frequencies of the cylinder made of T1N0.5, T1N1.0, T1N2.0 and T1N5.0 is presented in Fig. 12. It is obvious that by increasing the deformations, the natural frequencies become larger. It implies that the dynamic characteristics are sensitive to the large deformations, which should be considered in cylinder design.

The time histories of nonlinear radial displacement at point 'B' for Type 2 and various volume fraction indices is plotted in Fig. 13. It can be observed from this figure that the amplitude and period of vibration increase when the volume fraction index increases.

In Figs. 14 (a) and 14(b), the time histories of the cylinders made of T3N0.5 and T3N5.0 are plotted for various damping ratios. According to these figures one can conclude that as would be expected, by increasing the damping ratio, the rate of vibration decays will be increased. In addition, by comparing these figures it is obvious that the damping ratio has more effect on vibration decays for lower volume fraction indices.

The nonlinear radial displacement wave propagation along the radial direction at $z = L/2$ can be tracked in Figs. 15 (a) and 15(b) for T1N0.5 and T1N5.0, respectively.

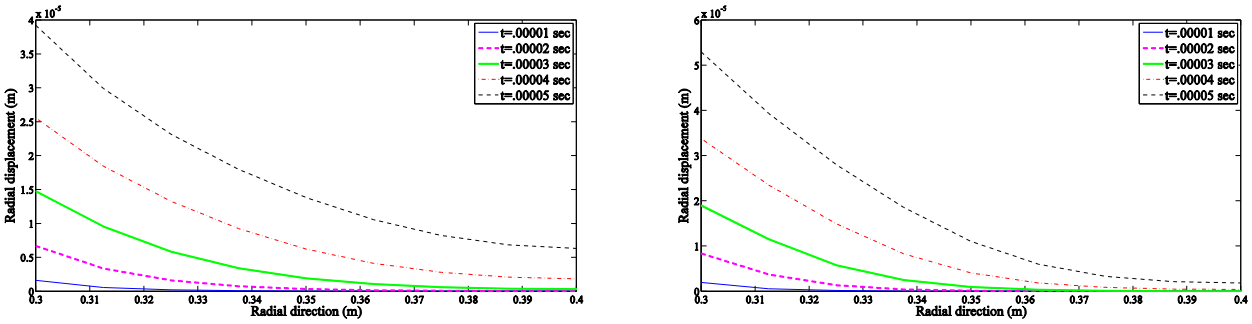

(a) T1N0.5 (b) T1N5.0

Fig. 15 The nonlinear radial displacement wave propagation along the radial direction for two volume fraction indices of Type 1

Table 4 The normalized higher natural frequencies ϖ_1 and ϖ_2 at the different time steps for various GPLs distribution patterns

Time step		Type 1				Type 2				Type 3			
		n=0.5	n=1.0	n=2.0	n=5.0	n=0.5	n=1.0	n=2.0	n=5.0	n=0.5	n=1.0	n=2.0	n=5.0
$t=0$	ϖ_1	0.3502	0.3215	0.2925	0.2668	0.3611	0.3371	0.3101	0.2811	0.3606	0.3385	0.3078	0.2762
	ϖ_2	0.3655	0.3364	0.3061	0.2742	0.3772	0.3518	0.3228	0.2854	0.3734	0.3424	0.3152	0.2825
$0.25\,t_0$	ϖ_1	0.3683	0.3427	0.3170	0.2983	0.3806	0.3588	0.3391	0.3124	0.3831	0.3559	0.3319	0.3085
	ϖ_2	0.3832	0.3551	0.3291	0.3012	0.3959	0.3727	0.3440	0.3164	0.3877	0.3663	0.3397	0.3110
$0.50\,t_0$	ϖ_1	0.3898	0.3598	0.3341	0.3165	0.4059	0.3806	0.3594	0.3360	0.4064	0.3790	0.3533	0.3306
	ϖ_2	0.4028	0.3724	0.3468	0.3246	0.4184	0.3938	0.3635	0.3384	0.4094	0.3828	0.3570	0.3330
$0.75\,t_0$	ϖ_1	0.4114	0.3778	0.3479	0.3314	0.4274	0.4076	0.3817	0.3507	0.4238	0.4014	0.3719	0.3469
	ϖ_2	0.4233	0.3938	0.3618	0.3409	0.4382	0.4178	0.3850	0.3577	0.4337	0.4074	0.3752	0.3493
$1.00\,t_0$	ϖ_1	0.4177	0.4014	0.3607	0.3425	0.4363	0.4253	0.4067	0.3663	0.4337	0.4199	0.3944	0.3599
	ϖ_2	0.4351	0.4071	0.3783	0.3493	0.4500	0.4293	0.4093	0.3749	0.4433	0.4229	0.3973	0.3632

In these figures the radial displacement wave front can be tracked at various time instants. The distance between the graphs at the different times represents the speed of wave propagation. Comparing these figures reveals that the volume fraction index has significant effect on wave propagation. The wave propagation speed increased with the volume fraction index decreasing.

9. Conclusions

The MLPG method for the geometrically nonlinear vibration analysis of FG graphene platelets-reinforced nanocomposite cylinder is presented. The radial point interpolation method is employed to discretize the problem domain. The energy dissipation is taken in to account using the Rayleigh damping matrix. The distribution of GPLs along the radial direction is described by a micromechanical model based on the Halpin-Tsai model and rule of mixture. First, the accuracy of present MLPG method is corroborated via comparisons with the results obtained by FEM with very fine meshing and a good agreement is achieved for '8×40' nodal distribution. Then, it is demonstrated that the results of the MLPG method is more stable compared with the FEM one's because of eliminating the mesh distortion issue. Finally, various types of GPLRR-FG nanocomposite cylinders have been analyzed using the proposed method and influence of reinforcement of the cylinder by GPLs with various grading patterns on stiffness, natural frequencies and periods of vibration are discussed in details. Moreover, the effect of Rayleigh damping of cylinder on the nonlinear vibration responses is studied. The important results can be outlined as follows:

- The results showed that the GPLRR-FG nanocomposite cylinders have higher stiffness, strength and natural frequencies compared to isotropic polymer cylinder.
- The stiffness and strength of the GPLRR-FG increases with the decrease of volume fraction index for all distribution pattern types.
- In particular, the T1N0.5 GPLRR-FG nanocomposite offers the best compromise in terms of strength and stiffness.
- The normalized natural frequencies increase along with the decreasing the volume fraction index. The most increasing in natural frequencies comparing with the isotropic polymer cylinder with proportions of 51 to 54%

is achieved for T2N0.5 nanocomposite cylinder.

- It showed that the large deformations, effects on stiffness and dynamic characteristics such as natural frequencies, amplitude and period of vibration. For example under uniform internal pressure, by increasing the deformations, the natural frequencies become larger and the amplitude of vibration becomes smaller.
- Increasing the volume fraction index causes to larger amplitude and period of vibration.
- The damping ratio has more effect on vibration decays in lower volume fraction indices.
- Volume fraction index has significant effect on wave propagation. The wave propagation speed increased with the volume fraction index decreasing.
- Although the MLPG method needs more computational cost compared to the FEM, but it does not need the computational cost in the pre-processing which is usually more expensive. Additionally based on the obtained results, the MLPG method yields to more accurate results especially in large deformations compared to the FEM which must be considered together with the computational cost.

References

Arefi, M., Mohammadi, M., Tabatabaeian, A., Dimitri, R. and Tornabene, F. (2018), "Two-dimensional thermo-elastic analysis of FG-CNTRC cylindrical pressure vessels", *Steel Compos. Struct.*, **27**(4), 525-536. https://doi.org/10.12989/scs.2018.27.4.525.

Bouguenina, O., Belakhdar, K., Tounsi, A. and Adda Bedia, E.A. (2015), "Numerical analysis of FGM plates with variable thickness subjected to thermal buckling", *Steel Compos. Struct.*, **19**(3), 679-695. https://dx.doi.org/10.12989/scs.2015.19.3.679.

Bui, T.Q., Nguyen, N.T., Van Lich, L., Nguyen, M.N. and Truong, T.T. (2018), "Analysis of transient dynamic fracture parameters of cracked functionally graded composites by improved meshfree methods", *Theor. Appl. Fract. Mech.*, **96**, 642-657. https://doi.org/10.1016/j.tafmec.2017.10.005.

Celigoj, C.C. (2001), "An improved 'assumed enhanced displacement gradient'ring-element for finite deformation axisymmetric and torsional problems", *Int. J. Numer. Method. Eng.*, **50**(4), 899-918. https://doi.org/10.1002/1097-0207(20010210)50:4<899::AID-NME58>3.0.CO;2-Y.

Chen, D., Yang, J. and Kitipornchai, S. (2017), "Nonlinear vibration and postbuckling of functionally graded graphene reinforced porous nanocomposite beams", *Compos. Sci. Technol.*, **142**, 235-245. https://doi.org/10.1016/j.compscitech.2017.02.008.

Chen, J.S., Pan, C. and Wu, C.T. (1997), "Large deformation analysis of rubber based on a reproducing kernel particle method", *Comput. Mech.*, **19**(3), 211-227. https://doi.org/10.1007/s004660050170.

Chu, F., He, J., Wang, L. and Zhong, Z. (2016), "Buckling analysis of functionally graded thin plate with in-plane material inhomogeneity", *Eng. Anal. with Bound. Elem.*, **65**, 112-125. https://doi.org/10.1016/j.enganabound.2016.01.007.

Feng, C., Kitipornchai, S. and Yang, J. (2017). "Nonlinear free vibration of functionally graded polymer composite beams reinforced with graphene nanoplatelets (GPLs)", *Eng. Struct.*, **140**, 110-119. https://doi.org/10.1016/j.engstruct.2017.02.052.

Ferezghi, Y.S., Sohrabi, M.R. and MosaviNezhad, S.M. (2018), "Dynamic analysis of non-symmetric FG cylindrical shell under shock loading by using MLPG method", *Struct. Eng. Mech.*, **67**(6), 659-669. https://doi.org/10.12989/sem.2018.67.6.659.

Ghayoumizadeh, H., Shahabian, F. and Hosseini, S.M. (2013), "Elastic wave propagation in a functionally graded nanocomposite reinforced by carbon nanotubes employing meshless local integral equations (LIEs)", *Eng. Anal. Bound. Elem.*, **37**(11), 1524-1531. https://doi.org/10.1016/j.enganabound.2013.08.011.

Gu, Y., Wang, Q.X. and Lam, K.Y. (2007), "A meshless local Kriging method for large deformation analyses", *Comput. Method. Appl. M.*, **196**(9-12), 1673-1684. https://doi.org/10.1016/j.cma.2006.09.017.

Gupta, N. (2007), "A functionally graded syntactic foam material for high energy absorption under compression", *Mater. Lett.*, **61**(4-5), 979-982. https://doi.org/10.1016/j.matlet.2006.06.033.

Hajnayeb, A. and Khadem, S.E. (2015), "An analytical study on the nonlinear vibration of a double-walled carbon nanotube", *Struct. Eng. Mech.*, **54**(5), 987-998. https://dx.doi.org/10.12989/sem.2015.54.5.987.

Hasselman, D.P.H. and Youngblood, G.E. (1978), "Enhanced thermal stress resistance of structural ceramics with thermal conductivity gradient", *J. Am. Ceramic Soc.*, **61**(1-2), 49-52. https://doi.org/10.1111/j.1151-2916.1978.tb09228.x.

Hosseini, S.M. and Zhang, C. (2018), "Elastodynamic and wave propagation analysis in a FG graphene platelets-reinforced nanocomposite cylinder using a modified nonlinear micromechanical model", *Steel Compos. Struct.*, **27**(3), 255-271. https://doi.org/10.12989/scs.2018.27.3.255.

Hosseini, S. M., Sladek, J. and Sladek, V. (2015). "Two dimensional analysis of coupled non-Fick diffusion-elastodynamics problems in functionally graded materials using meshless local Petrov–Galerkin (MLPG) method", *Appl. Math. Comput.*, **268**, 937-946. https://doi.org/10.1016/j.amc.2015.07.009.

Kawasaki, A. and Watanabe, R. (2002). "Thermal fracture behavior of metal/ceramic functionally graded materials", *Eng. Fract. Mech.*, **69**(14-16), 1713-1728. https://doi.org/10.1016/S0013-7944(02)00054-1.

Khayat, M., Poorveis, D. and Moradi, S. (2017), "Buckling analysis of functionally graded truncated conical shells under external displacement-dependent pressure", *Steel Compos. Struct.*, **23**(1), 1-16. https://doi.org/10.12989/scs.2017.23.1.001.

Kitipornchai, S., Chen, D. and Yang, J. (2017), "Free vibration and elastic buckling of functionally graded porous beams reinforced by graphene platelets", *Mater. Design*, **116**, 656-665. https://doi.org/10.1016/j.matdes.2016.12.061.

Kou, K.P. and Yang, Y. (2019), "A meshfree boundary-domain integral equation method for free vibration analysis of the functionally graded beams with open edged cracks", *Compos. Part B: Eng.*, **156**, 303-309. https://doi.org/10.1016/j.compositesb.2018.08.089.

Krahulec, S., Sladek, J., Sladek, V. and Hon, Y.C. (2016), "Meshless analyses for time-fractional heat diffusion in functionally graded materials", *Eng. Anal. with Bound. Elem.*, **62**, 57-64. https://doi.org/10.1016/j.enganabound.2015.09.008.

Lee, W.Y., Stinton, D.P., Berndt, C.C., Erdogan, F., Lee, Y.D. and Mutasim, Z. (1996), "Concept of functionally graded materials for advanced thermal barrier coating applications", *J. Am. Ceramic Soc.*, **79**(12), 3003-3012. https://doi.org/10.1111/j.1151-2916.1996.tb08070.x

Lei, Z.X., Zhang, L.W. and Liew, K.M. (2016), "Buckling analysis of CNT reinforced functionally graded laminated composite

plates", *Compos. Struct.*, **152**, 62-73. https://doi.org/10.1016/j.compstruct.2016.05.047.

Lei, Z.X., Zhang, L.W. and Liew, K.M. (2017), "Meshless modeling of geometrically nonlinear behavior of CNT-reinforced functionally graded composite laminated plates", *Appl. Math. Comput.*, **295**, 24-46. https://doi.org/10.1016/j.amc.2016.09.017.

Li, C. and Weng, G.J. (2002), "Antiplane crack problem in functionally graded piezoelectric materials", *J. Appl. Mech.*, **69**(4), 481-488. https://doi.org/10.1115/1.1467091.

Li, K., Wu, D., Chen, X., Cheng, J., Liu, Z., Gao, W. and Liu, M. (2018). "Isogeometric Analysis of functionally graded porous plates reinforced by graphene platelets", *Compos. Struct.*, **204**, 114-130. https://doi.org/10.1016/j.compstruct.2018.07.059.

Liew, K.M., Lei, Z.X. and Zhang, L.W. (2015), "Mechanical analysis of functionally graded carbon nanotube reinforced composites: a review", *Compos. Struct.*, **120**, 90-97. https://doi.org/10.1016/j.compstruct.2014.09.041.

Lin, J., Li, J., Guan, Y., Zhao, G., Naceur, H. and Coutellier, D. (2018), "Geometrically nonlinear bending analysis of functionally graded beam with variable thickness by a meshless method", *Compos. Struct.*, **189**, 239-246. https://doi.org/10.1016/j.compstruct.2018.01.063.

Liu, D., Kitipornchai, S., Chen, W. and Yang, J. (2018), "Three-dimensional buckling and free vibration analyses of initially stressed functionally graded graphene reinforced composite cylindrical shell", *Compos. Struct.*, **189**, 560-569. https://doi.org/10.1016/j.compstruct.2018.01.106.

Liu, Z.S., Swaddiwudhipong, S. and Koh, C.G. (2002), "Stress wave propagation in 1-D and 2-D media using smooth particle hydrodynamics method", *Struct. Eng. Mech.*, **14**(4), 455-472. https://doi.org/10.12989/sem.2002.14.4.455.

Mirzaei, M. and Kiani, Y. (2017). "Isogeometric thermal buckling analysis of temperature dependent FG graphene reinforced laminated plates using NURBS formulation", *Compos. Struct.*, **180**, 606-616. https://doi.org/10.1016/j.compstruct.2017.08.057.

Mohammadimehr, M., Arshid, E., Alhosseini, S.M.A.R., Amir, S. and Arani, M.R.G. (2019), "Free vibration analysis of thick cylindrical MEE composite shells reinforced CNTs with temperature-dependent properties resting on viscoelastic foundation", *Struct. Eng. Mech.*, **70**(6), 683-702. https://doi.org/10.12989/sem.2019.70.6.683.

Nguyen, T.N., Thai, C.H., Luu, A.T., Nguyen-Xuan, H. and Lee, J. (2019), "NURBS-based postbuckling analysis of functionally graded carbon nanotube-reinforced composite shells", *Comput. Method. Appl. M.,* **347**, 983-1003. https://doi.org/10.1016/j.cma.2019.01.011.

Nguyen, T.N., Thai, C.H., Nguyen-Xuan, H. and Lee, J. (2018), "Geometrically nonlinear analysis of functionally graded material plates using an improved moving Kriging meshfree method based on a refined plate theory", *Compos. Struct.*, **193**, 268-280. https://doi.org/10.1016/j.compstruct.2018.03.036.

Ocylok, S., Weisheit, A. and Kelbassa, I. (2010), "Functionally graded multi-layers by laser cladding for increased wear and corrosion protection", *Phys. Procedia*, **5**, 359-367. https://doi.org/10.1016/j.phpro.2010.08.157.

Rad, M.H.G., Shahabian, F. and Hosseini, S.M. (2015a), "A meshless local Petrov–Galerkin method for nonlinear dynamic analyses of hyper-elastic FG thick hollow cylinder with Rayleigh damping", *Acta Mechanica*, **226**(5), 1497-1513. https://doi.org/10.1007/s00707-014-1266-2.

Rad, M.H.G., Shahabian, F. and Hosseini, S. M. (2015b), "Large deformation hyper-Elastic modeling for nonlinear dynamic analysis of two dimensional functionally graded domains using the meshless local Petrov-Galerkin (MLPG) method", *CMES: Comput. Model. Eng. Sci.*, **108**(3), 135-157. https://doi.org/10.3970/cmes.2015.108.135.

Rad, M.H.G., Shahabian, F. and Hosseini, S.M. (2015c), "Geometrically nonlinear elastodynamic analysis of hyper-elastic neo-Hooken FG cylinder subjected to shock loading using MLPG method", *Eng. Anal. with Bound. Eelem.*, **50**, 83-96. https://doi.org/10.1016/j.enganabound.2014.08.002.

Rad, M.H.G., Shahabian, F. and Hosseini, S.M. (2019), "Nonlocal geometrically nonlinear dynamic analysis of nanobeam using a meshless method", *Steel Compos. Struct.*, **32**(3), 293-304. https://doi.org/10.12989/scs.2019.32.3.293.

Reddy, J.N. (2014), *An Introduction to Nonlinear Finite Element Analysis: With Applications to Heat Transfer, Fluid Mechanics, and Solid Mechanics*. OUP Oxford, Texas, USA.

Sahmani, S., Aghdam, M.M. and Rabczuk, T. (2018), "Nonlinear bending of functionally graded porous micro/nano-beams reinforced with graphene platelets based upon nonlocal strain gradient theory", *Compos. Struct.*, **186**, 68-78.
https://doi.org/10.1016/j.compstruct.2017.11.082

Schulz, U., Peters, M., Bach, F.W. and Tegeder, G. (2003), "Graded coatings for thermal, wear and corrosion barriers", *Mater. Sci. Eng.: A*, **362**(1-2), 61-80. https://doi.org/10.1016/S0921-5093(03)00579-3.

Shi, Z.A. and Chen, Y. (2004), "Functionally graded piezoelectric cantilever beam under load", *Arch. Appl. Mech.*, **74**(3-4), 237-247. https://doi.org/10.1007/s00419-004-0346-5.

Sladek, J., Sladek, V., Stanak, P., Zhang, C. and Wünsche, M. (2013), "Analysis of the bending of circular piezoelectric plates with functionally graded material properties by a MLPG method", *Eng. Struct.*, **47**, 81-89. https://doi.org/10.1016/j.engstruct.2012.02.034.

Sladek, V., Sladek, J., Tanaka, M. and Zhang, C. (2005). "Transient heat conduction in anisotropic and functionally graded media by local integral equations", *Eng. Anal. with Bound. Elem.*, **29**(11), 1047-1065. https://doi.org/10.1016/j.enganabound.2005.05.011.

Soltanimaleki, A., Foroutan, M. and Alihemmati, J. (2016), "Free vibration analysis of functionally graded fiber reinforced cylindrical panels by a three dimensional mesh-free model", *J. Vib. Control*, **22**(19), 4087-4098. https://doi.org/10.1177/1077546315570717.

Thai, C.H., Do, V.N. and Nguyen-Xuan, H. (2016), "An improved Moving Kriging-based meshfree method for static, dynamic and buckling analyses of functionally graded isotropic and sandwich plates", *Eng. Anal. with Bound. Elem.*, **64**, 122-136. https://doi.org/10.1016/j.enganabound.2015.12.003.

Thai, C.H., Ferreira, A.J.M. and Phung-Van, P. (2019b), "Size dependent free vibration analysis of multilayer functionally graded GPLRC microplates based on modified strain gradient theory". *Compos. Part B: Eng.*, **169**, 174-188. https://doi.org/10.1016/j.compositesb.2019.02.048.

Thai, C.H., Ferreira, A.J.M., Rabczuk, T. and Nguyen-Xuan, H. (2018b), "A naturally stabilized nodal integration meshfree formulation for carbon nanotube-reinforced composite plate analysis". *Eng. Anal. Bound. Elem.*, **92**, 136-155. https://doi.org/10.1016/j.enganabound.2017.10.018.

Thai, C.H., Ferreira, A.J.M., Tran, T.D. and Phung-Van, P. (2019a), "Free vibration, buckling and bending analyses of multilayer functionally graded graphene nanoplatelets reinforced composite plates using the NURBS formulation". *Compos. Struct.*, **220**, 749-759. https://doi.org/10.1016/j.compstruct.2019.03.100.

Thai, C.H., Ferreira, A.J.M., Tran, T.D. and Phung-Van, P. (2019c), "A size-dependent quasi-3D isogeometric model for functionally graded graphene platelet-reinforced composite microplates based on the modified couple stress theory". *Compos. Struct.*, 111695. https://doi.org/10.1016/j.compstruct.2019.111695.

Thai, C.H., Ferreira, A.J.M., Wahab, M.A. and Nguyen-Xuan, H. (2018a), "A moving Kriging meshfree method with naturally stabilized nodal integration for analysis of functionally graded material sandwich plates". *Acta Mechanica*, **229**(7), 2997-3023. https://doi.org/10.1007/s00707-018-2156-9.

Tutuncu, N. and Ozturk, M. (2001), "Exact solutions for stresses in functionally graded pressure vessels", *Compos. Part B: Eng.*, **32**(8), 683-686. https://doi.org/10.1016/S1359-8368(01)00041-5.

Vaghefi, R., Hematiyan, M.R. and Nayebi, A. (2016), "Three-dimensional thermo-elastoplastic analysis of thick functionally graded plates using the meshless local Petrov–Galerkin method", *Eng. Anal. with Bound. Elem.*, **71**, 34-49. https://doi.org/10.1016/j.enganabound.2016.07.001.

Verma, D., Gope, P.C., Shandilya, A. and Gupta, A. (2014), "Mechanical-thermal-electrical and morphological properties of graphene reinforced polymer composites: A review", *Transact. Indian Inst. Metals*, **67**(6), 803-816. https://doi.org/10.1007/s12666-014-0408-5.

Wang, H. and Qin, Q.H. (2008), "Meshless approach for thermo-mechanical analysis of functionally graded materials", *Eng. Anal. with Bound. Elem.*, **32**(9), 704-712. https://doi.org/10.1016/j.enganabound.2007.11.001.

Wu, C. P. and Liu, Y. C. (2016). "A state space meshless method for the 3D analysis of FGM axisymmetric circular plates", *Steel Compos. Struct.*, **22**(1), 161-182. https://doi.org/10.12989/scs.2016.22.1.161.

Xu, Y., Li, Z. and Guo, K. (2018), "Active vibration robust control for FGM beams with piezoelectric layers", *Struct. Eng. Mech.*, **67**(1), 33-43. https://doi.org/10.12989/sem.2018.67.1.033.

Yang, J., Wu, H. and Kitipornchai, S. (2017), "Buckling and postbuckling of functionally graded multilayer graphene platelet-reinforced composite beams", *Compos. Struct.*, **161**, 111-118. https://doi.org/10.1016/j.compstruct.2016.11.048.

Zhang, N., Khan, T., Guo, H., Shi, S., Zhong, W. and Zhang, W. (2019), "Functionally graded materials: An overview of stability, buckling, and free vibration analysis", *Adv. Mater. Sci. Eng.*, 2019. https://doi.org/10.1155/2019/1354150.

Zhu, P. and Liew, K.M. (2011), "Free vibration analysis of moderately thick functionally graded plates by local Kriging meshless method", *Compos. Struct.*, **93**(11), 2925-2944. https://doi.org/10.1016/j.compstruct.2011.05.011.

Zienkiewicz, O.C. and Taylor, R.L. (2005), *The Finite Element Method for Solid and Structural Mechanics*, Elsevier, United Kingdom.

CC